

# Python I, II, and III CMB Anisotropy Measurement Constraints on Open and Flat- $\Lambda$ CDM Cosmologies

Graça Rocha<sup>1,2</sup>, Radosław Stompor<sup>3,4</sup>, Ken Ganga<sup>5</sup>, Bharat Ratra<sup>1</sup>, Stephen R. Platt<sup>6</sup>, Naoshi Sugiyama<sup>7</sup>, and Krzysztof M. Górski<sup>8,9</sup>

## ABSTRACT

We use Python I, II, and III cosmic microwave background anisotropy data to constrain cosmologies. We account for the Python beamwidth and calibration uncertainties. We consider open and spatially-flat- $\Lambda$  cold dark matter cosmologies, with nonrelativistic-mass density parameter  $\Omega_0$  in the range 0.1–1, baryonic-mass density parameter  $\Omega_B$  in the range  $(0.005\text{--}0.029)h^{-2}$ , and age of the universe  $t_0$  in the range (10–20) Gyr. Marginalizing over all parameters but  $\Omega_0$ , the combined Python data favors an open (spatially-flat- $\Lambda$ ) model with  $\Omega_0 \simeq 0.2$  (0.1). At the  $2\sigma$  confidence level model normalizations deduced from the combined Python data are mostly consistent with those drawn from the DMR, UCSB South Pole 1994, ARGO, MAX 4 and 5, White Dish, and SuZIE data sets.

*Subject headings:* cosmic microwave background—cosmology: observations—large-scale structure of the universe

## 1. Introduction

Ganga et al. (1997a, hereafter GRGS) developed a technique to account for uncertainties, such as those in the beamwidth and the calibration, in likelihood analyses of cosmic microwave

---

<sup>1</sup>Department of Physics, Kansas State University, Manhattan, KS 66506.

<sup>2</sup>Centro de Astrofísica da Universidade do Porto, Rua das Estrelas s/n, 4100 Porto, Portugal.

<sup>3</sup>Center for Particle Astrophysics, University of California, Berkeley, CA 94720.

<sup>4</sup>Copernicus Astronomical Center, Bartycka 18, 00-716 Warszawa, Poland.

<sup>5</sup>Infrared Processing and Analysis Center, MS 100-22, California Institute of Technology, Pasadena, CA 91125.

<sup>6</sup>Snow and Ice Research Group, University of Nebraska, Lincoln, NE 68583-0850.

<sup>7</sup>Department of Physics, Kyoto University, Kitashirakawa-Oiwakecho, Sakyo-ku, Kyoto 606-8502, Japan.

<sup>8</sup>Theoretical Astrophysics Center, Juliane Maries Vej 30, 2100 Copenhagen Ø, Denmark.

<sup>9</sup>Warsaw University Observatory, Aleje Ujazdowskie 4, 00-478 Warszawa, Poland.

background (CMB) anisotropy data. This technique has been used in conjunction with theoretically-predicted CMB anisotropy spectra in analyses of the Gundersen et al. (1995) UCSB South Pole 1994 data, the Church et al. (1997) SuZIE data, the MAX 4+5 data (Tanaka et al. 1996; Lim et al. 1996), the Tucker et al. (1993) White Dish data, and the de Bernardis et al. (1994) ARGO data (GRGS; Ganga et al. 1997b, 1998; Ratra et al. 1998, 1999a, hereafter R99a). A combined analysis of all these data sets is presented in Ratra et al. (1999b, hereafter R99b).

In this paper we present a similar analysis of CMB anisotropy data from the Python I, II, and III observations performed at the South Pole (Dragovan et al. 1994, hereafter D94; Ruhl et al. 1995b, hereafter R95; Platt et al. 1997, hereafter P97). The Python detectors and telescope are described by Ruhl (1993) and D94; also see Ruhl et al. (1995a) and Alvarez (1996). In what follows we review the information needed for our analysis.

Python I, II, and III CMB data were taken in a frequency band centered at 90 GHz with four bolometric detectors centered at the corners of a  $2^{\circ}.75$  by  $2^{\circ}.75$  square on the sky. The beam profiles are well-approximated by a Gaussian of FWHM  $0^{\circ}.75 \pm 0^{\circ}.05$  (one standard deviation uncertainty). Observations were centered at  $\alpha = 23^{\text{h}}37$ ,  $\delta = -49^{\circ}.44$  (J2000.0). Python I and II data were taken at a single telescope elevation. Python III data were taken at this fiducial elevation as well as two additional elevations offset  $2^{\circ}.75/3$  on the sky above and below the fiducial elevation. The reduced Python data are shown in Figure 1.

All of the Python measurements were made by switching the four beams horizontally across the sky in a three-point pattern by rotating a vertical flat mirror at 2.5 Hz. This chopping pattern was then combined with slow (typically 0.1 Hz) azimuthal beam switching of the entire telescope to produce a four-beam response to a sky signal.

The chopper throw and azimuthal telescope beam switching were both  $2^{\circ}.75$  on the sky for the Python I and II observations. Python I (hereafter I) resulted in 16 data points, 8 each from the lower and upper rows of detectors (D94). Python II observed two sets of points on the sky (R95), although one of the detectors did not work during this season. The first set of observations, hereafter IIA, overlapped the I points and yielded 7 measurements from the lower row of detectors and 8 from the upper row. The second set, hereafter IIB, measured the same number of points on the sky as the first set, but these were offset in azimuth relative to the I points by  $-2^{\circ}.75/2$  on the sky.

Two series of measurements were made at each of the three elevations observed during the Python III season (P97). For each series, the physical throw of the chopper was the same at all elevations. Because the actual throw on the sky depends on elevation, the Python III beam was smeared to a Gaussian FWHM of  $0^{\circ}.82 \pm 0^{\circ}.05$  (one standard deviation uncertainty) when forming the four-beam pattern to account for the imperfect overlap of the beams caused by this effect. This procedure also accounted for the relative pointing uncertainty and fluctuations in the chopper throw.

The first series of Python III measurements, hereafter IIIL, used the same chopper and beam

switch parameters as Python I and II. The IIII data consists of two sets of points taken at the I elevation but offset in right ascension by  $-2^{\circ}75/3$  and  $-2 \times 2^{\circ}75/3$  on the sky. Two sets of measurements were also made at each of the lower and upper elevations, but these were offset in right ascension by  $0^{\circ}0$  and  $+2 \times 2^{\circ}75/3$  on the sky relative to I.

The second series of Python III measurements, hereafter IIIS, were made with both the chopper throw and telescope beam switch reduced to  $2^{\circ}75/3$ . For each of the three telescope elevations, the IIIS data consists of points separated horizontally by  $2^{\circ}75/3$  on the sky for each of the 2 rows of detectors. Figure 1 shows the points observed by IIII and IIIS at each elevation. Together, I, II, and III densely sample a  $5^{\circ}5$  by  $22^{\circ}$  region of the sky.

The  $1 \sigma$  absolute calibration uncertainty in the Python data is 20% (D94; R95; P97) and is accounted for in our analysis. The absolute pointing uncertainty is  $0^{\circ}1$  (D94; R95) and is not accounted for in our analysis.

In §2 we summarize the computational techniques used in our analysis. See GRGS and R99a for detailed discussions. Results are presented and discussed in §3. Conclusions are given in §4.

## 2. Summary of Computation

The zero-lag window function for the Python observations are shown in Figure 2 and the zero-lag window function parameters are in Table 1.

In this paper we focus on a spatially open CDM model and a spatially flat CDM model with a cosmological constant  $\Lambda$ . These low density models are largely consistent with current observational constraints.<sup>10</sup> For recent discussions see Park et al. (1998), Retzlaff et al. (1998), Croft et al. (1999), and Peebles (1999).

The models have Gaussian, adiabatic primordial energy-density power spectra. The flat- $\Lambda$  model CMB anisotropy computations use a scale-invariant energy-density perturbation power spectrum (Harrison 1970; Peebles & Yu 1970; Zel’dovich 1972), as predicted in the simplest spatially-flat inflation models (Guth 1981; Kazanas 1980; Sato 1981). The open model computations use the energy-density power spectrum (Ratra & Peebles 1994, 1995; Bucher, Goldhaber, & Turok 1995; Yamamoto, Sasaki, & Tanaka 1995) predicted in the simplest open-bubble inflation models (Gott 1982). The computation of the CMB anisotropy spectra is described by Stompor (1994) and Sugiyama (1995).

As discussed in R99a, the spectra are parameterized by their quadrupole-moment amplitude

---

<sup>10</sup> While not considered in this paper, a time-variable cosmological “constant” dominated spatially-flat model is also largely consistent with current data (e.g., Peebles & Ratra 1988; Sugiyama & Sato 1992; Ratra & Quillen 1992; Frieman & Waga 1998; Ferreira & Joyce 1998; Wang & Steinhardt 1998; Carroll 1998; Hu et al. 1999; Huterer & Turner 1999; Liddle & Scherrer 1999; Starobinsky 1998).

$Q_{\text{rms-PS}}$ , the nonrelativistic-mass density parameter  $\Omega_0$ , the baryonic-mass density parameter  $\Omega_B$ , and the age of the universe  $t_0$ . The spectra are computed for a range of  $\Omega_0$  spanning the interval 0.1 to 1 in steps of 0.1, for a range of  $\Omega_B h^2$  [the Hubble parameter  $h = H_0/(100 \text{ km s}^{-1} \text{ Mpc}^{-1})$ ] spanning the interval 0.005 to 0.029 in steps of 0.004, and for a range of  $t_0$  spanning the interval 10 to 20 Gyr in steps of 2 Gyr. In total 798 spectra were computed to cover the cosmological-parameter spaces of the open and flat- $\Lambda$  models. Figure 2 shows examples of the CMB anisotropy spectra used in our analysis. Other examples are in Figure 2 of R99a and Figure 1 of R99b.

While it is of interest to also consider other cosmological parameters, such as tilt or gravity wave fraction or a time-variable cosmological “constant” (instead of a constant  $\Lambda$ ), to make the problem tractable we have focussed on the four parameters mentioned above. We emphasize however that the results of the analysis are model dependent. For instance, a time-variable  $\Lambda$  model would likely lead to a different constraint on  $\Omega_0$  than that derived below in the constant  $\Lambda$  model.

Following GRGS, for each of the 798 spectra considered the “bare” likelihood function is computed at the nominal beamwidth and calibration, as well as at a number of other values of the beamwidth and calibration determined from the measurement uncertainties. The likelihood function used in the derivation of the central values and limits is determined by integrating (marginalizing) the bare likelihood function over the beamwidth and calibration uncertainties with weights determined by the measured probability distribution functions of the beamwidth and the calibration. See GRGS for a more detailed discussion. When marginalizing over the beamwidth uncertainty we have checked in a few selected cases that the five-point Gauss-Hermite quadrature summation approximation to the integral agrees extremely well with the three-point Gauss-Hermite approximation used by GRGS (and for most of the analysis in this paper). The likelihoods are a function of four parameters mentioned above:  $Q_{\text{rms-PS}}$ ,  $\Omega_0$ ,  $\Omega_B h^2$ , and  $t_0$ . We also compute marginalized likelihood functions by integrating over one or more of these parameters after assuming a uniform prior in the relevant parameters. The prior is set to zero outside the ranges considered for the parameters. GRGS and R99a describe the prescription used to determine central values and limits from the likelihood functions. In what follows we consider 1, 2, and 3  $\sigma$  highest posterior density limits which include 68.3, 95.4, and 99.7% of the area.

### 3. Results and Discussion

Table 2 lists the derived values of  $Q_{\text{rms-PS}}$  and bandtemperature  $\delta T_l$  for the flat bandpower spectrum, for various combinations of the I, II, and III data. These numerical values account for the beamwidth and calibration uncertainties. The last two  $\delta T_l$  entries in Table 2 are quite consistent with those derived by P97; the small differences reflect the different methods used to account for beamwidth and calibration uncertainties here and in P97.

For the flat bandpower spectrum the combined I, II, and III data average  $1 \sigma \delta T_l$  error bar is  $\sim 25\%$ <sup>11</sup> : Python data results in a very significant detection of CMB anisotropy, even after accounting for beamwidth and calibration uncertainties. Note that the calibration uncertainty, 20%, is the most important contributor to this error bar.

A number of other interesting conclusions follow from the entries in Table 2. Comparing the I+II and III results, which are from experiments which probe almost identical angular scales, we see that the III amplitude is  $\sim 1 \sigma$  higher than the I+II amplitude. Comparing the result from the analysis of the coadded I and IIA data (which are from experiments with identical window functions) and the result from the full analysis of the I and IIA data (which takes into account all the spatial correlations), we see that the deduced amplitudes are almost identical. This is probably mostly a reflection of the fact that the individual I and IIA amplitudes are almost identical (see Table 2).

As discussed in R99a and R99b, the four-dimensional posterior probability density distribution function  $L(Q_{\text{rms-PS}}, \Omega_0, \Omega_B h^2, t_0)$  is nicely peaked in the  $Q_{\text{rms-PS}}$  direction but fairly flat in the other three directions. Marginalizing over  $Q_{\text{rms-PS}}$  results in a three-dimensional posterior distribution  $L(\Omega_0, \Omega_B h^2, t_0)$  which is steeper, but still relatively flat. As a consequence, limits derived from the four- and three-dimensional posterior distributions are generally not highly statistically significant. We therefore do not show contour plots of these functions here. Marginalizing over  $Q_{\text{rms-PS}}$  and one other parameter results in two-dimensional posterior probability distributions which are more peaked. See Figures 3 and 4. As in the ARGO (R99a) and combination (R99b) data set analyses, in some cases these peaks are at an edge of the parameter range considered.

Figure 3 shows that the two-dimensional posterior distributions allow one to distinguish between different regions of parameter space at a fairly high formal level of confidence. For instance, the open model near  $\Omega_0 \sim 0.75$ ,  $\Omega_B h^2 \sim 0.03$ , and  $t_0 \sim 20$  Gyr, and the flat- $\Lambda$  model near  $\Omega_0 \sim 0.6$ ,  $\Omega_B h^2 \sim 0.03$ , and  $t_0 \sim 20$  Gyr, are both formally ruled out at  $\sim 3 \sigma$  confidence. However, we emphasize, as discussed in R99a and R99b, care must be exercised when interpreting the discriminative power of these formal limits, since they depend sensitively on the fact that the uniform prior has been set to zero outside the range of the parameter space we have considered.

Figure 4 shows the contours of the two-dimensional posterior distribution for  $Q_{\text{rms-PS}}$  and  $\Omega_0$ , derived by marginalizing the four-dimensional distribution over  $\Omega_B h^2$  and  $t_0$ . These are shown for the combined Python I, II, and III data, the DMR data, and three combinations of data from the SP94, ARGO, MAX 4+5, White Dish, and SuZIE experiments (R99b), for both the open and flat- $\Lambda$  models. Constraints on these parameters from the combined Python data are consistent with those from the DMR data for the flat- $\Lambda$  models, panel *a*), while for the open model, panel *b*),

---

<sup>11</sup> For comparison, the corresponding DMR  $1 \sigma \delta T_l$  error bar is  $\sim 10 - 12\%$  (depending on model, Górski et al. 1998).

consistency at  $2\sigma$  ( $1\sigma$ ) requires  $\Omega_0 \gtrsim 0.2$  (0.35). The combined Python data amplitudes are a little higher than those derived from the other small-scale data combinations, panels  $c) - h)$ , but at  $2\sigma$  confidence the various amplitudes are mostly consistent.

Figure 5 shows the one-dimensional posterior distribution functions for  $\Omega_0$ ,  $\Omega_B h^2$ ,  $t_0$ , and  $Q_{\text{rms-PS}}$ , derived by marginalizing the four-dimensional posterior distribution over the other three parameters. From these one-dimensional distributions, the combined I, II, and III data favors an open (flat- $\Lambda$ ) model with  $\Omega_0 = 0.19$  (0.10), or  $\Omega_B h^2 = 0.005$  (0.005), or  $t_0 = 10$  (13) Gyr, amongst the models considered. At  $2\sigma$  confidence the combined Python data formally rule out only small regions of parameter space. From the one-dimensional distributions of Figure 5, the data requires  $\Omega_0 < 0.71$  or  $> 0.8$  ( $\Omega_0 < 0.55$  or  $> 0.63$ ), or  $\Omega_B h^2 < 0.028$  ( $\Omega_B h^2 < 0.028$ ), or  $t_0 < 20$  Gyr ( $t_0 < 20$  Gyr) for the open (flat- $\Lambda$ ) model at  $2\sigma$ . As discussed in R99a and R99b, care is needed when interpreting the discriminative power of these formal limits. These papers also discuss a more conservative Gaussian posterior distribution limit prescription. Using this more conservative prescription, we find only an upper  $1\sigma$  limit on  $\Omega_0$  ( $\lesssim 0.5$ ) in the open model.

While the statistical significance of the constraints on cosmological parameters is not high, it is reassuring that the combined Python data favor low-density, low  $\Omega_B h^2$ , young models, consistent with some of the indications from the combinations of CMB anisotropy data considered by R99b, and the indications from most recent non-CMB observations (see discussion in R99b).

The peak values of the one-dimensional posterior distributions shown in Figure 5 are listed in the figure caption for the case when the four-dimensional posterior distributions are normalized such that  $L(Q_{\text{rms-PS}} = 0 \mu\text{K}) = 1$ . With this normalization, marginalizing over the remaining parameter the fully marginalized posterior distributions are  $2 \times 10^{106} (1 \times 10^{106})$  for the open (flat- $\Lambda$ ) model and the combined Python data. This is qualitatively consistent with the indication from panels  $a)$  and  $b)$  of Figure 5 that the most-favored open model is somewhat more favored than the most-favored flat- $\Lambda$  one.

#### 4. Conclusion

The combined Python I, II, and III data results derived here are mostly consistent with those derived from the DMR, SP94, ARGO, MAX 4+5, White Dish and SuZIE data. The combined Python data significantly constrains  $Q_{\text{rms-PS}}$  (for the flat bandpower spectrum  $Q_{\text{rms-PS}} = 40_{-8}^{+12} \mu\text{K}$  at  $1\sigma$ ) and weakly favors low-density, low  $\Omega_B h^2$ , young models.

We acknowledge helpful discussions with D. Alvarez, M. Dragovan, G. Griffin, J. Kovac, and J. Ruhl. This work was partially carried out at the Infrared Processing and Analysis Center and the Jet Propulsion Laboratory, California Institute of Technology, under a contract with the National Aeronautics and Space Administration. KG also acknowledges support from NASA ADP grant NASA-1260. BR and GR acknowledge support from NSF grant EPS-9550487 with matching

support from the state of Kansas and from a K\*STAR First award. GR also acknowledges support from a PRAXIS XXI program of FCT (Portugal) grant. RS acknowledges support from NASA AISRP grant NAG-3941 and help from Polish Scientific Committee (KBN) grant 2P03D00813.

Table 1: Numerical Values for the Zero-Lag Window Function Parameters<sup>a</sup>

	$l_{e^{-0.5}}$	$l_e$	$l_m$	$l_{e^{-0.5}}$	$\sqrt{I(W_l)}$
Python I/II	53	91.7	73	99	1.34
Python IIIL	52	87.7	72	98	1.30
Python IIIS	128	171	176	230	0.623

<sup>a</sup>The value of  $l$  where  $W_l$  is largest,  $l_m$ , the two values of  $l$  where  $W_{l_{e^{-0.5}}} = e^{-0.5}W_{l_m}$ ,  $l_{e^{-0.5}}$ , the effective multipole,  $l_e = I(lW_l)/I(W_l)$ , and  $I(W_l) = \sum_{l=2}^{\infty} (l+0.5)W_l/\{l(l+1)\}$ .

Table 2: Numerical Values for  $Q_{\text{rms-PS}}$  and  $\delta T_l$  from Likelihood Analyses Assuming a Flat Bandpower Spectrum

Data Set <sup>a</sup>	$Q_{\text{rms-PS}}^{\text{b}}$ ( $\mu\text{K}$ )	Ave. Abs. Err. <sup>c</sup> ( $\mu\text{K}$ )	Ave. Frac. Err. <sup>d</sup>	$\delta T_l^{\text{b}}$ ( $\mu\text{K}$ )	LR <sup>e</sup>
I	39 $\begin{smallmatrix} 56 \\ 28 \end{smallmatrix}$	14	36%	61 $\begin{smallmatrix} 87 \\ 43 \end{smallmatrix}$	$2 \times 10^{14}$
IIA	39 $\begin{smallmatrix} 57 \\ 27 \end{smallmatrix}$	15	38%	60 $\begin{smallmatrix} 88 \\ 43 \end{smallmatrix}$	$9 \times 10^{12}$
C(I+IIA)	40 $\begin{smallmatrix} 57 \\ 29 \end{smallmatrix}$	14	35%	62 $\begin{smallmatrix} 89 \\ 45 \end{smallmatrix}$	$3 \times 10^{31}$
I+IIA	40 $\begin{smallmatrix} 56 \\ 29 \end{smallmatrix}$	14	35%	61 $\begin{smallmatrix} 87 \\ 45 \end{smallmatrix}$	$2 \times 10^{31}$
IIB <sup>f</sup>	9.3 $\begin{smallmatrix} 20 \\ 0 \end{smallmatrix}$	10	110%	14 $\begin{smallmatrix} 31 \\ 0 \end{smallmatrix}$	1
II	31 $\begin{smallmatrix} 44 \\ 23 \end{smallmatrix}$	10	34%	48 $\begin{smallmatrix} 68 \\ 35 \end{smallmatrix}$	$1 \times 10^{12}$
C(I+IIA)+IIB	34 $\begin{smallmatrix} 47 \\ 26 \end{smallmatrix}$	11	31%	53 $\begin{smallmatrix} 73 \\ 40 \end{smallmatrix}$	$1 \times 10^{30}$
I+II	34 $\begin{smallmatrix} 46 \\ 25 \end{smallmatrix}$	11	31%	52 $\begin{smallmatrix} 72 \\ 39 \end{smallmatrix}$	$1 \times 10^{30}$
IIIL	41 $\begin{smallmatrix} 55 \\ 32 \end{smallmatrix}$	11	28%	64 $\begin{smallmatrix} 84 \\ 49 \end{smallmatrix}$	$3 \times 10^{33}$
IIIS	42 $\begin{smallmatrix} 56 \\ 33 \end{smallmatrix}$	11	27%	66 $\begin{smallmatrix} 87 \\ 51 \end{smallmatrix}$	$2 \times 10^{29}$
III	41 $\begin{smallmatrix} 54 \\ 33 \end{smallmatrix}$	10	25%	64 $\begin{smallmatrix} 83 \\ 51 \end{smallmatrix}$	$6 \times 10^{68}$
I+II+IIIL	39 $\begin{smallmatrix} 51 \\ 31 \end{smallmatrix}$	10	27%	60 $\begin{smallmatrix} 80 \\ 47 \end{smallmatrix}$	$3 \times 10^{67}$
I+II+III	40 $\begin{smallmatrix} 52 \\ 32 \end{smallmatrix}$	10	25%	63 $\begin{smallmatrix} 81 \\ 50 \end{smallmatrix}$	$1 \times 10^{105}$

<sup>a</sup>C(...+...) means that the data from the two sets of observations have been coadded prior to analysis, II refers to the combined IIA and IIB data, and III refers to the combined IIIL and IIIS data.

<sup>b</sup>For each data set, the first of the three entries is where the posterior probability density distribution function peaks and the vertical pair of numbers are the  $\pm 1 \sigma$  (68.3% highest posterior density) values.

<sup>c</sup>Average absolute error on  $Q_{\text{rms-PS}}$  in  $\mu\text{K}$ .

<sup>d</sup>Average fractional error, as a fraction of the central value.

<sup>e</sup>Likelihood ratio.

<sup>f</sup>IIB does not have a  $2 \sigma$  highest posterior density detection; the appropriate equal tail  $2 \sigma$  upper limits are  $50 \mu\text{K}$  ( $Q_{\text{rms-PS}}$ ) and  $77 \mu\text{K}$  ( $\delta T_l$ ).

## REFERENCES

- Alvarez, D.L. 1996, Princeton University Ph.D. Thesis
- Bucher, M., Goldhaber, A.S., & Turok, N. 1995, *Phys. Rev. D*, 52, 3314
- Carroll, S.M. 1998, *Phys. Rev. Lett.*, 81, 3067
- Church, S.E., Ganga, K.M., Ade, P.A.R., Holzzapfel, W.L., Mauskopf, P.D., Wilbanks, T.M., & Lange, A.E. 1997, *ApJ*, 484, 523
- Croft, R.A.C., Weinberg, D.H., Pettini, M., Hernquist, L., & Katz, N. 1999, *ApJ*, in press
- de Bernardis, P., et al. 1994, *ApJ*, 422, L33
- Dragovan, M., Ruhl, J.E., Novak, G., Platt, S.R., Crone, B., Pernic, R., & Peterson, J.B. 1994, *ApJ*, 427, L67 (D94)
- Ferreira, P.G., & Joyce, M. 1998, *Phys. Rev. D*, 58, 023503
- Frieman, J.A., & Waga, I. 1998, *Phys. Rev. D*, 57, 4642
- Ganga, K., Ratra, B., Church, S.E., Sugiyama, N., Ade, P.A.R., Holzzapfel, W.L., Mauskopf, P.D., & Lange, A.E. 1997b, *ApJ*, 484, 517
- Ganga, K., Ratra, B., Gundersen, J.O., & Sugiyama, N. 1997a, *ApJ*, 484, 7 (GRGS)
- Ganga, K., Ratra, B., Lim, M.A., Sugiyama, N., & Tanaka, S.T. 1998, *ApJS*, 114, 165
- Górski, K.M., Ratra, B., Stompor, R., Sugiyama, N., & Banday, A.J. 1998, *ApJS*, 114, 1
- Gott, J.R. 1982, *Nature*, 295, 304
- Gundersen, J.O., et al. 1995, *ApJ*, 443, L57
- Guth, A. 1981, *Phys. Rev. D*, 23, 347
- Harrison, E.R. 1970, *Phys. Rev. D*, 1, 2726
- Hu, W., Eisenstein, D.J., Tegmark, M., & White, M. 1999, *Phys. Rev. D*, 59, 023512
- Huterer, D., & Turner, M.S. 1999, *Phys. Rev. Lett.*, submitted
- Kazanas, D. 1980, *ApJ*, 241, L59
- Liddle, A.R., & Scherrer, R.J. 1999, *Phys. Rev. D*, 59, 023509
- Lim, M.A., et al. 1996, *ApJ*, 469, L69
- Park, C., Colley, W.N., Gott, J.R., Ratra, B., Spergel, D.N., & Sugiyama, N. 1998, *ApJ*, 506, 473
- Peebles, P.J.E. 1999, *PASP*, 111, 274
- Peebles, P.J.E., & Ratra, B. 1988, *ApJ*, 325, L17
- Peebles, P.J.E., & Yu, J.T. 1970, *ApJ*, 162, 815
- Platt, S.R., Kovac, J., Dragovan, M., Peterson, J.B., & Ruhl, J.E. 1997, *ApJ*, 475, L1 (P97)

- Ratra, B., Ganga, K., Stompor, R., Sugiyama, N., de Bernardis, P., & Górski, K.M. 1999a, *ApJ*, 510, 11 (R99a)
- Ratra, B., Ganga, K., Sugiyama, N., Tucker, G.S., Griffin, G.S., Nguyễn, H.T., & Peterson, J.B. 1998, *ApJ*, 505, 8
- Ratra, B., & Peebles, P.J.E. 1994, *ApJ*, 432, L5
- Ratra, B., & Peebles, P.J.E. 1995, *Phys. Rev. D*, 52, 1837
- Ratra, B., & Quillen, A. 1992, *MNRAS*, 259, 738
- Ratra, B., Stompor, R., Ganga, K., Rocha, G., Sugiyama, N., & Górski, K.M. 1999b, *ApJ*, 517, in press (R99b)
- Retzlaff, J., Borgani, S., Gottlöber, S., Klypin, A., & Müller, V. 1998, *New Astron.*, 3, 631
- Ruhl, J. 1993, Princeton University Ph.D. Thesis
- Ruhl, J.E., Dragovan, M., Novak, G., Platt, S.R., Crone, B.K., & Pernic, R.W. 1995a, *Astro. Lett. and Comm.*, 32, 249
- Ruhl, J.E., Dragovan, M., Platt, S.R., Kovac, J., & Novak, G. 1995b, *ApJ*, 453, L1 (R95)
- Sato, K. 1981, *Phys. Lett. B*, 99, 66
- Starobinsky, A.A. 1998, *JETP Lett.*, 68, 757
- Stompor, R. 1994, *A&A*, 287, 693
- Stompor, R. 1997, in *Microwave Background Anisotropies*, ed. F.R. Bouchet, R. Gispert, B. Guiderdoni, & J. Tran Thanh Van (Gif-sur-Yvette: Editions Frontieres), 91
- Sugiyama, N. 1995, *ApJS*, 100, 281
- Sugiyama, N., & Sato, K. 1992, *ApJ*, 387, 439
- Tanaka, S.T., et al. 1996, *ApJ*, 468, L81
- Tucker, G.S., Griffin, G.S., Nguyễn, H.T., & Peterson, J.B. 1993, *ApJ*, 419, L45
- Wang, L., & Steinhardt, P.J. 1998, *ApJ*, 508, 483
- Yamamoto, K., Sasaki, M., & Tanaka, T. 1995, *ApJ*, 455, 412
- Zel'dovich, Ya. B. 1972, *MNRAS*, 160, 1P

### Figure Captions

Fig. 1.– Measured thermodynamic temperature differences (with  $\pm 1\text{-}\sigma$  error bars). Panel *a*) shows Python I (open circles), IIA (filled squares, offset horizontally from true positions for clarity), IIB (open squares), and IIIL (crosses) data, while panel *b*) shows Python IIIS data (crosses).

Fig. 2.– CMB anisotropy multipole moments  $l(l+1)C_l/(2\pi) \times 10^{10}$  (solid lines, scale on left axis, note that these are fractional anisotropy moments and thus dimensionless) as a function of multipole  $l$ , for selected models normalized to the DMR maps (Górski et al. 1998; Stompor 1997). Panels *a*) – *c*) show selected flat- $\Lambda$  models. The heavy lines are the  $\Omega_0 = 0.1$ ,  $\Omega_B h^2 = 0.005$ , and  $t_0 = 12$  Gyr case, which is close to where the combined Python data likelihoods (marginalized over all but one parameter at a time) are at a maximum. Panel *a*) shows five  $\Omega_B h^2 = 0.005$ ,  $t_0 = 12$  Gyr models with  $\Omega_0 = 0.1, 0.3, 0.5, 0.7,$  and  $0.9$  in descending order at the  $l \sim 200$  peaks. Panel *b*) shows seven  $\Omega_0 = 0.1$ ,  $t_0 = 12$  Gyr models with  $\Omega_B h^2 = 0.029, 0.025, 0.021, 0.017, 0.013, 0.009,$  and  $0.005$  in descending order at the  $l \sim 200$  peaks. Panel *c*) shows six  $\Omega_0 = 0.1$ ,  $\Omega_B h^2 = 0.005$  models with  $t_0 = 20, 18, 16, 14, 12,$  and  $10$  Gyr in descending order at the  $l \sim 200$  peaks. Panels *d*) – *f*) show selected open models. The heavy lines are the  $\Omega_0 = 0.2$ ,  $\Omega_B h^2 = 0.005$ , and  $t_0 = 10$  Gyr case, which is close to where the combined Python data likelihoods (marginalized over all but one parameter at a time) are at a maximum. Panel *d*) shows five  $\Omega_B h^2 = 0.005$ ,  $t_0 = 10$  Gyr models with  $\Omega_0 = 1, 0.8, 0.6, 0.4,$  and  $0.2$  from left to right at the peaks (the peak of the  $\Omega_0 = 0.2$  model is off scale). Panel *e*) shows seven  $\Omega_0 = 0.2$ ,  $t_0 = 10$  Gyr models with  $\Omega_B h^2 = 0.029, 0.025, 0.021, 0.017, 0.013, 0.009,$  and  $0.005$  in descending order at  $l \sim 400$ . Panel *f*) shows six  $\Omega_0 = 0.2$ ,  $\Omega_B h^2 = 0.005$  models with  $t_0 = 20, 18, 16, 14, 12,$  and  $10$  Gyr in descending order at  $l \sim 400$ . Also shown are the Python zero-lag window functions  $W_l$  (scale on right axis): I/II (long-dashed lines), IIIL (short-dashed lines), and IIIS (dotted lines). See Table 1 for  $W_l$ -parameter values.

Fig. 3.– Confidence contours and maxima of the combined Python data two-dimensional posterior probability density distribution functions, as a function of the two parameters on the axes of each panel (derived by marginalizing the four-dimensional posterior distributions over the other two parameters). Dashed lines (crosses) show the contours (maxima) of the open case and solid lines (solid circles) show those of the flat- $\Lambda$  model. Panel *a*) shows the  $(\Omega_B h^2, \Omega_0)$  plane, and panel *b*) shows the  $(t_0, \Omega_0)$  plane.

Fig. 4.– Confidence contours and maxima of the two-dimensional  $(Q_{\text{rms-PS}}, \Omega_0)$  posterior probability density distribution functions. Panels *a*), *c*), *e*), & *g*) in the left column show the flat- $\Lambda$  model and panels *b*), *d*), *f*), & *h*) in the right column show the open model. Note the different scale on the vertical ( $Q_{\text{rms-PS}}$ ) axes of pairs of panels in each row. Heavy lines show the  $\pm 1$  and  $\pm 2 \sigma$  confidence limits and solid circles show the maxima of the two-dimensional posterior distributions derived from the combined Python I, II, and III data. Shaded regions show the two-dimensional posterior distribution  $1 \sigma$  (denser shading) and  $2 \sigma$  (less dense shading) confidence regions for the DMR data (Górski et al. 1998; Stompor 1997) in panels *a*) & *b*); for the SP94, ARGO, MAX 4

and 5, White Dish and SuZIE data combination (R99b) in panels *c*) & *d*); for the previous data combination excluding SuZIE (R99b) in panels *e*) & *f*); and for the SP94Ka, MAX 4 ID, and MAX 5 HR data combination (R99b) in panels *g*) & *h*). The DMR results are a composite of those from analyses of the two extreme data sets: i) galactic frame with quadrupole included and correcting for faint high-latitude galactic emission; and ii) ecliptic frame with quadrupole excluded and no other galactic emission correction (Górski et al. 1998). In panels *c*) – *h*) crosses show the maxima of the appropriate non-Python data two-dimensional posterior distributions.

Fig. 5.– One-dimensional posterior probability density distribution functions for  $\Omega_0$ ,  $\Omega_B h^2$ ,  $t_0$ , and  $Q_{\text{rms-PS}}$  (derived by marginalizing the four-dimensional one over the other three parameters) in the open and flat- $\Lambda$  models. These have been renormalized to unity at the peaks. Dotted vertical lines show the confidence limits derived from these one-dimensional posterior distributions and solid vertical lines in panels *g*) and *h*) show the  $\pm 1$  and  $\pm 2 \sigma$  confidence limits derived by projecting the combined Python I, II, and III data four-dimensional posterior distributions. The  $2 \sigma$  DMR (marginalized and projected) confidence limits in panels *g*) and *h*) are a composite of those from the two extreme DMR data sets (see caption of Figure 4). When the four-dimensional posterior distributions are normalized such that  $L(Q_{\text{rms-PS}} = 0 \mu\text{K}) = 1$ , the peak values of the one-dimensional distributions shown in panels *a*) – *h*) are  $2 \times 10^{106}$ ,  $3 \times 10^{106}$ ,  $6 \times 10^{107}$ ,  $7 \times 10^{107}$ ,  $1 \times 10^{105}$ ,  $2 \times 10^{105}$ ,  $9 \times 10^{104}$ , and  $6 \times 10^{104}$ , respectively.

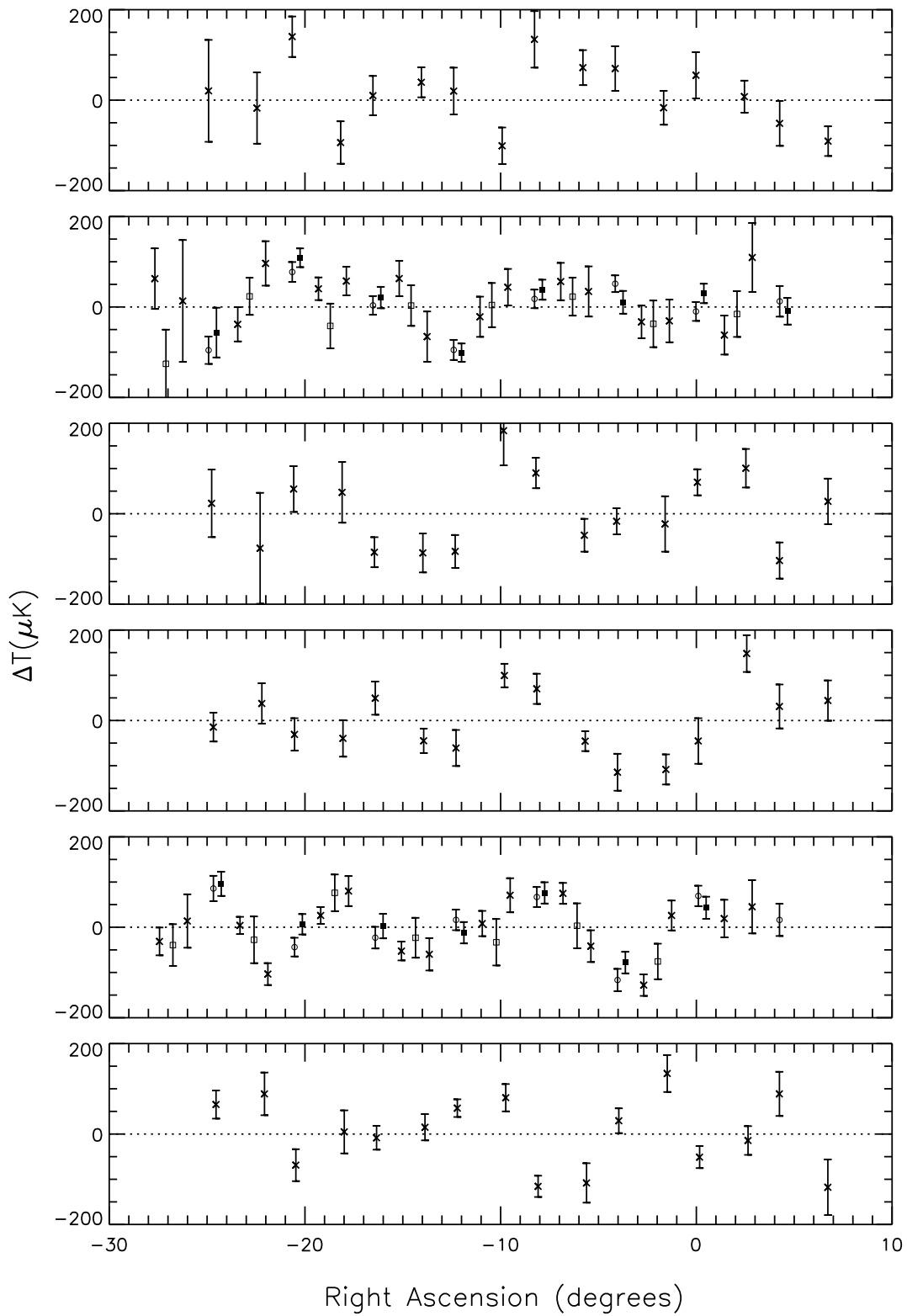


Figure 1a)

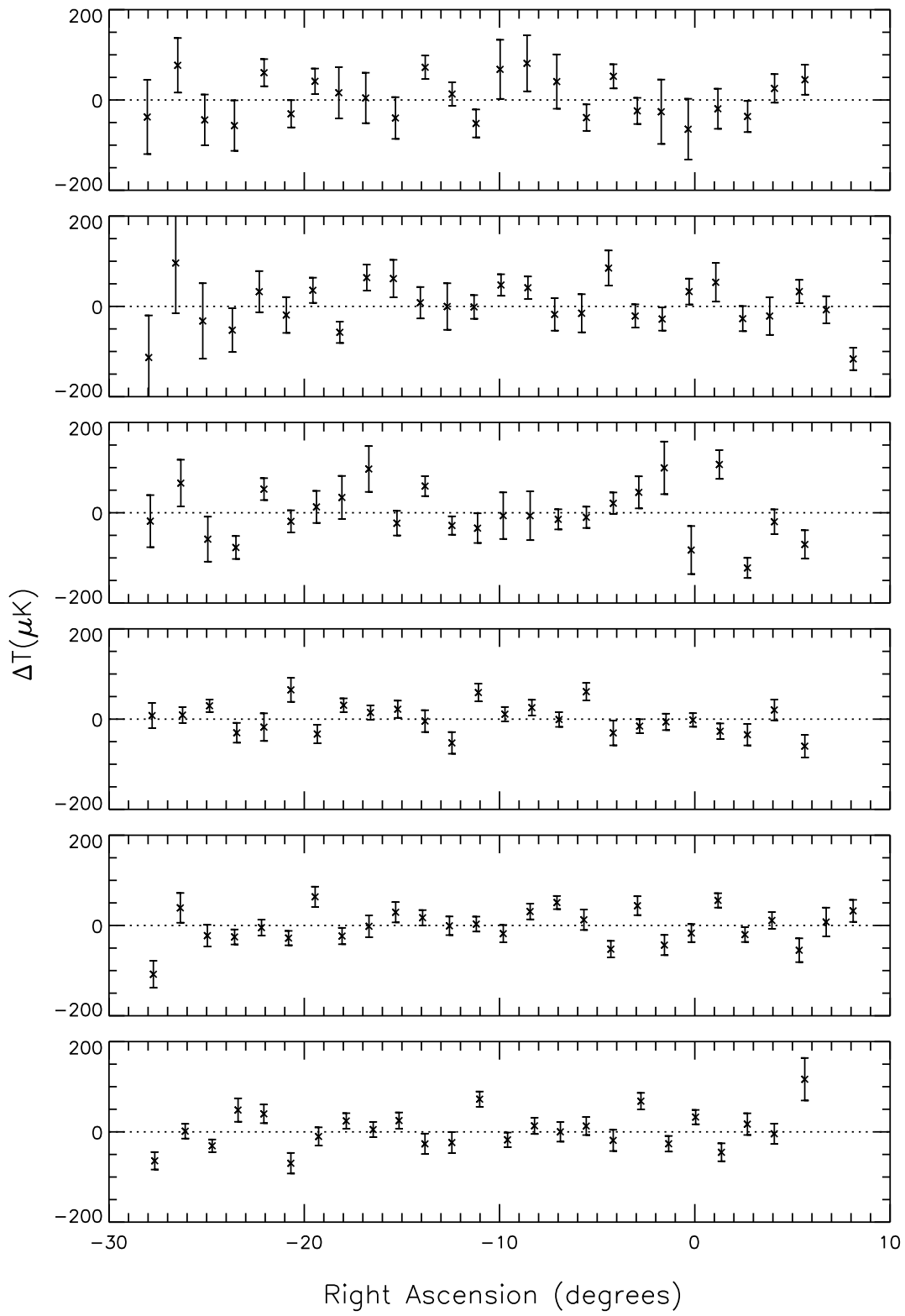


Figure 1b)

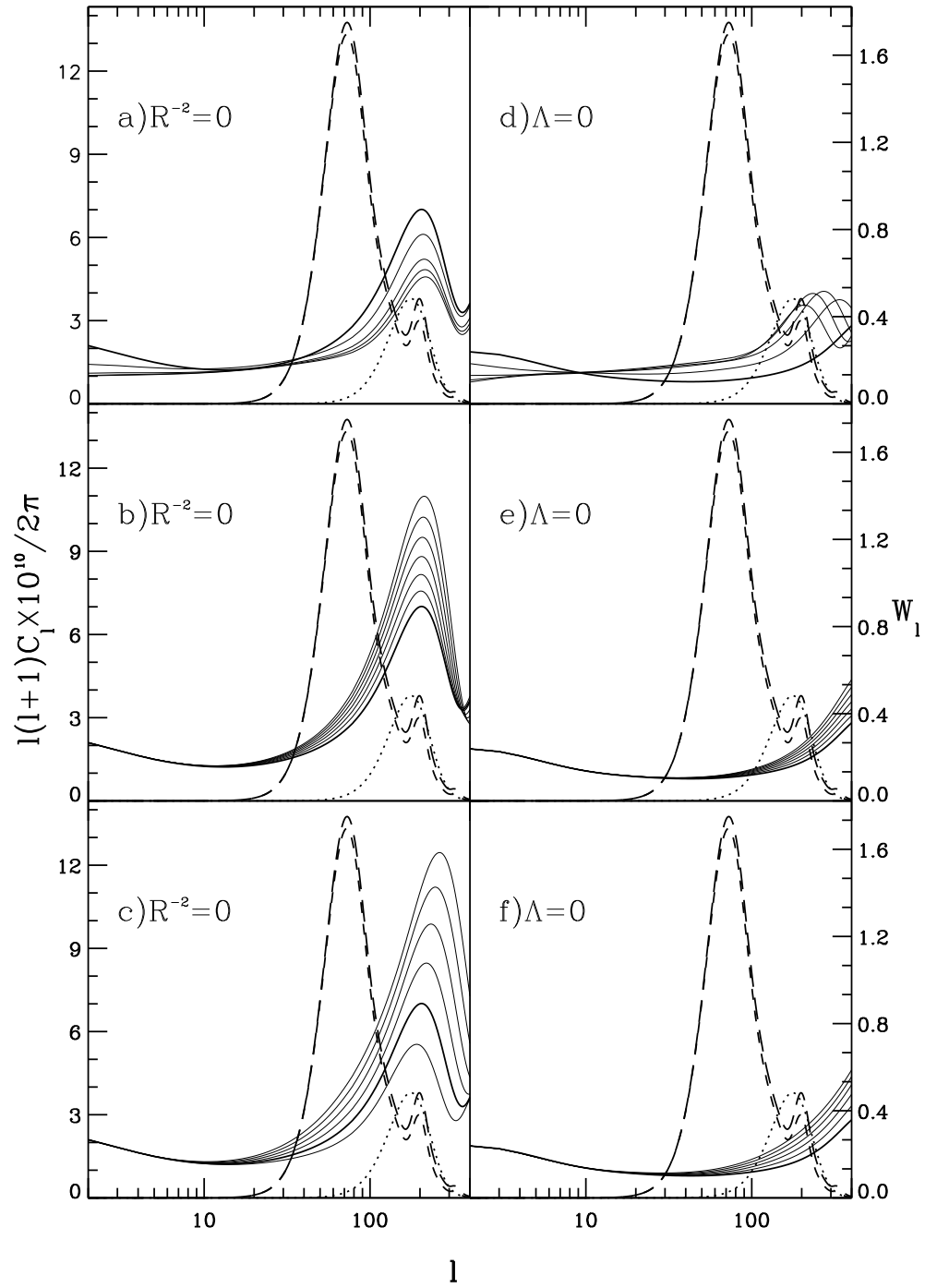


Figure 2

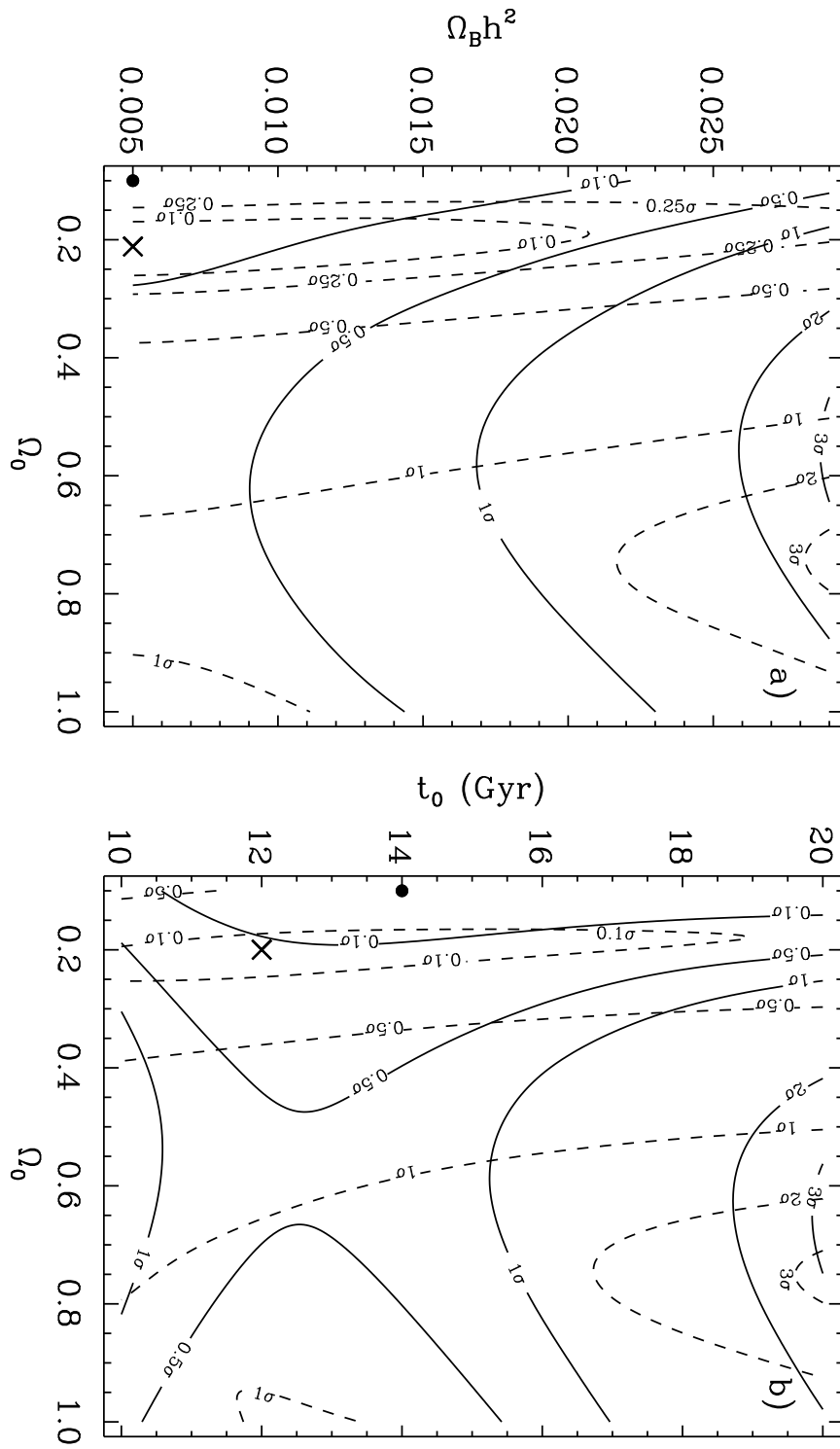


Figure 3

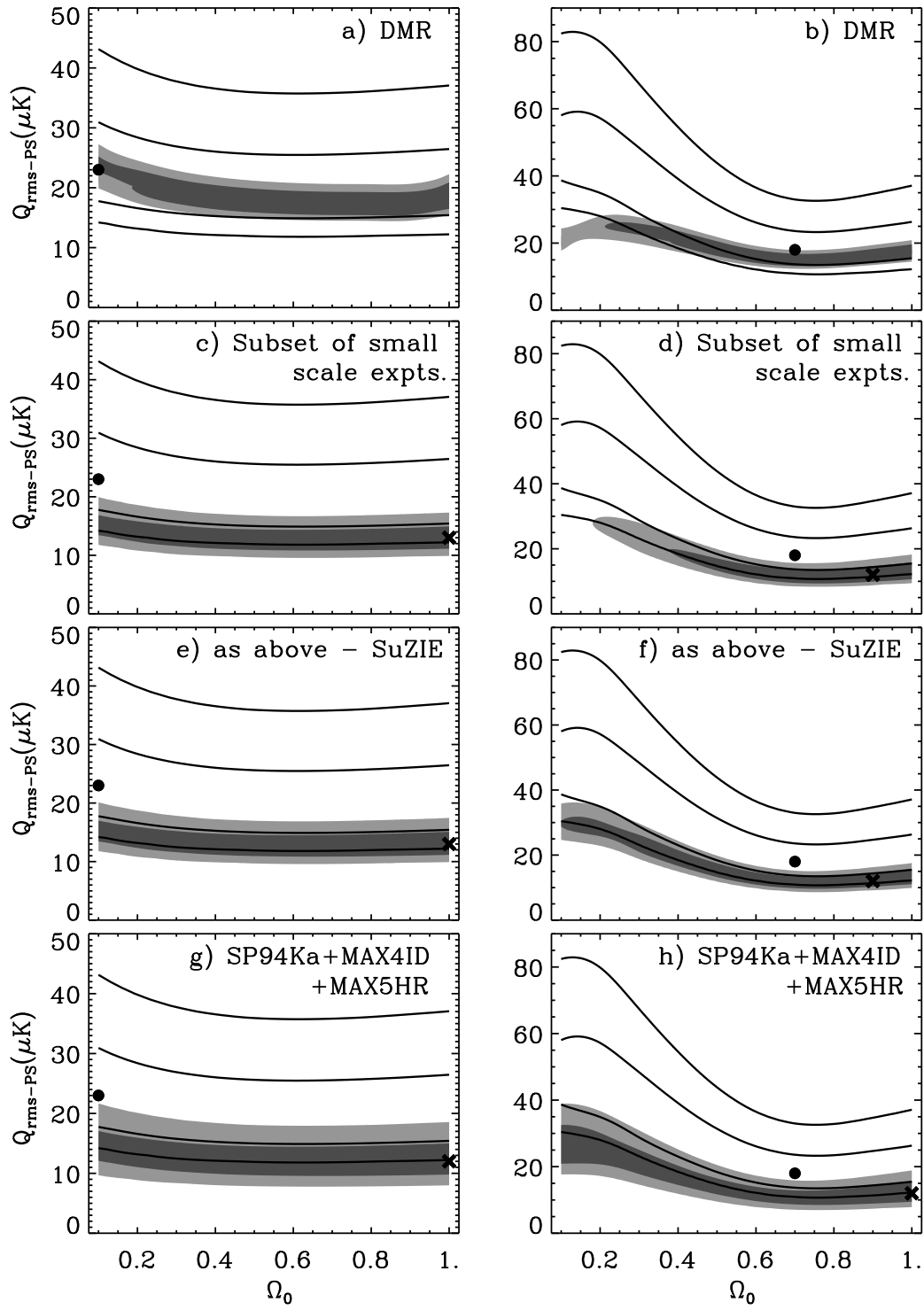


Figure 4

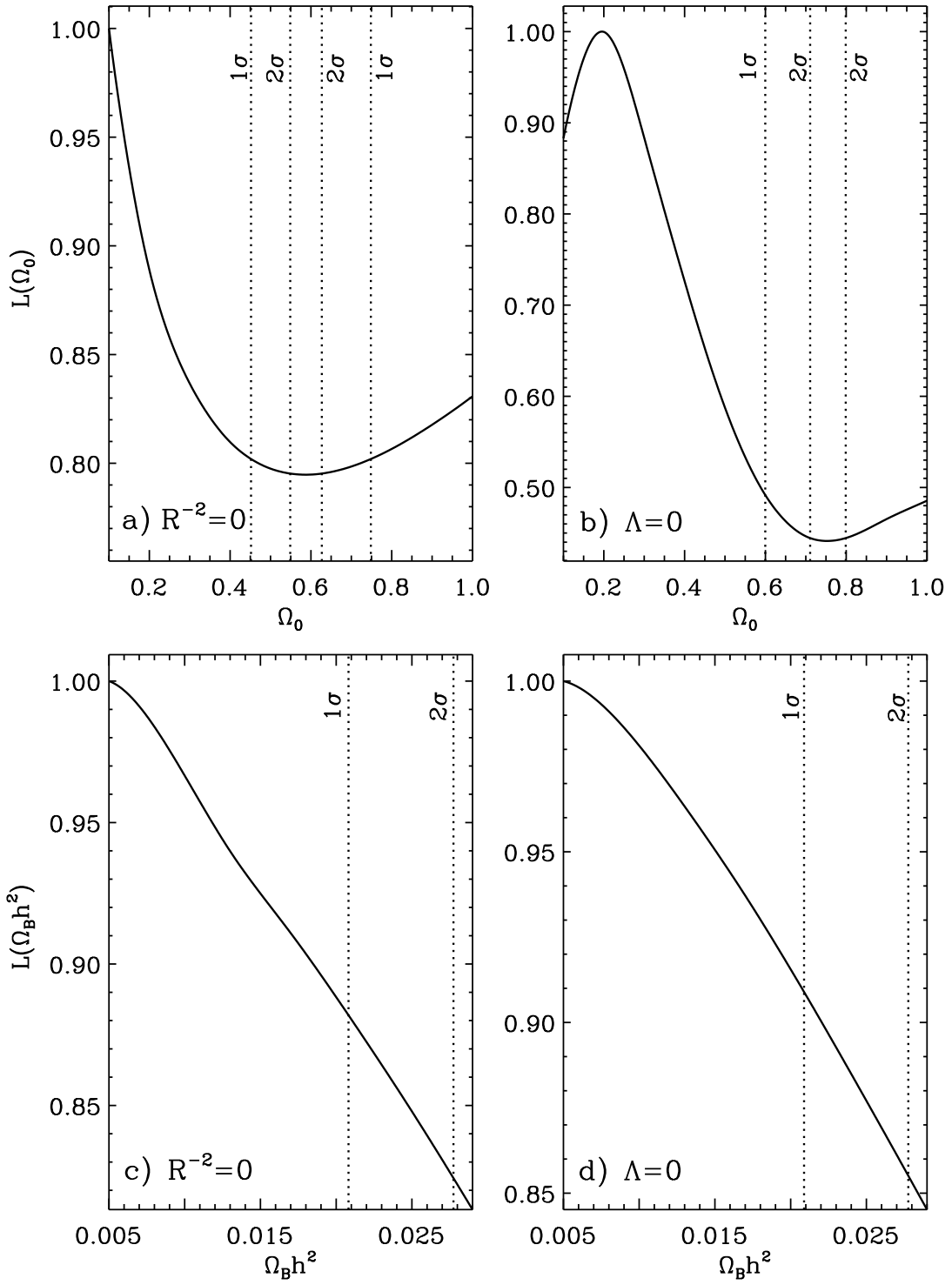


Figure 5.1

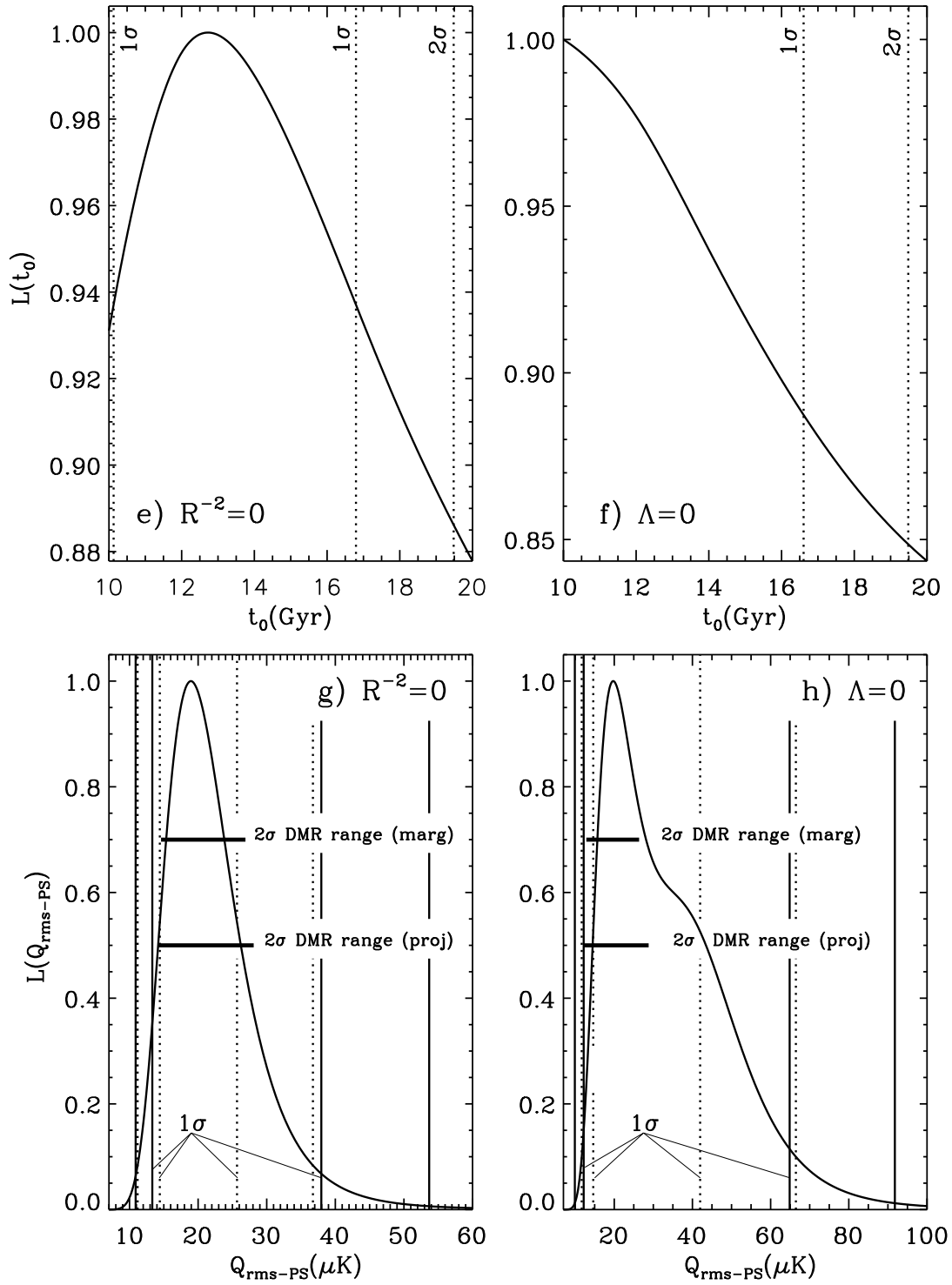


Figure 5.2